



# Shock Response of Polymethyl Methacrylate (PMMA) Under Explosive Loading

S. M. Torres<sup>1</sup> · M. J. Hargather<sup>1</sup> · J. Kimberley<sup>1</sup> · R. E. Robey<sup>2</sup>

Received: 25 August 2023 / Accepted: 4 March 2024  
© The Author(s) 2024

## Abstract

The dynamic response of polymethyl methacrylate (PMMA) is well understood for one-dimensional planar impact shocks, but limited research has been performed on the response of PMMA under spherical shock loading. In this work, the shock decay of an explosively-driven shock wave into PMMA was experimentally measured. PMMA cubes of various geometries were explosively loaded with an RP-80 detonator to produce the explosive shock wave. High-speed schlieren imaging was implemented to measure the explosively-driven shock wave velocity throughout the PMMA cubes. Photon Doppler velocimetry (PDV) was used to measure the particle velocity imparted by the shock wave at the surface of the cubes. The material shock response was studied at distances from 21.91 to 133.3 mm from the explosive source. The particle velocity history measured by PDV was compared to the wave profile visualized in the high-speed images. The shock wave pulse amplitude decreased with increased distance from the source. The conducted experiments extend the PMMA shock Hugoniot relating to the lower shock and particle velocity regime.

**Keywords** Polymethyl methacrylate (PMMA) · Hugoniot · Explosives · Photon Doppler velocimetry (PDV) · Schlieren imaging

## Introduction

Characterization of the shock response of polymethyl methacrylate (PMMA) has been carried out since the late 1960s [1–4]. The shock response of PMMA is of interest since PMMA is often used as a window material for interferometry techniques [5], or an attenuation material for explosive gap testing [6]. Understanding the material shock response not only benefits experiments but also better informs numerical simulations [6]. Extensive work has been conducted characterizing PMMA shock Hugoniots [7–9], the viscoelastic/viscoplastic response [5, 10], window corrections, and index of refraction [2, 11, 12]. PMMA research also extends

to the comparison of manufacturers [6, 10, 13] to understand variations in material characteristics. High-rate mechanical property relationships have been developed as reviewed in [14]. The shock response of PMMA was characterized using planar impact experiments or explosive plane-wave generators producing one-dimensional (1D) shock waves. However, limited research has been conducted to understand the explosive induced shock response of PMMA for spherical shock wave profiles.

Dynamic material characterization is typically achieved through planar impact experiments where manganin gauges and velocity interferometry are implemented [2, 5, 10, 15]. The shock arrival time at two gauge locations is used to determine shock velocity; the corresponding particle velocity is recorded using velocity interferometry. Measured shock parameters in PMMA yield a non-linear shock speed - particle velocity Hugoniot [2, 7, 10] which has been attributed to the viscoelastic/viscoplastic response of the material [5]. Further description of the viscoelastic/viscoplastic material response was explored by [5, 10] using lateral stress gauges where a reduction in lateral stress behind the shock wave was noted. Jordan et al. [10] determined the viscoelastic behavior to be prevalent

---

J. Kimberley is a member of SEM.

✉ S. M. Torres  
sivana.torres@student.nmt.edu

✉ M. J. Hargather  
michael.hargather@nmt.edu

<sup>1</sup> Mechanical Engineering, New Mexico Tech, 801 Leroy Pl., Socorro, NM 87801, USA

<sup>2</sup> Sandia National Labs, Albuquerque, NM 87185, USA

in the lower region of the shock Hugoniot whereas Millett and Bourne [5] measured the stress reduction both above and below the PMMA Hugoniot Elastic Limit (HEL) of approximately 0.75 GPa.

An alternative to measuring the shock velocity using manganin gauges is the implementation of high-speed imaging. The optical transparency of PMMA makes the implementation of high-speed imaging advantageous for the visualization of the material response [14]. The instantaneous increase in density imparted by a shock wave allows for visualization of the wave and its propagation. Previous research has shown that the Gladstone-Dale relation, which states that density is directly proportional to refractive index, describes the PMMA material response at pressures below 2 GPa [2, 11]. Refractive imaging techniques such as schlieren and shadowgraphy [9] can thus be leveraged to visualize shock propagation [16]. High-speed schlieren imaging is used primarily in the gas phase, with extensive application to shock wave measurements including extracting quantitative air shock density profiles [17, 18], but has also been implemented to measure shock Hugoniot of optically transparent solid materials [9]. Streak cameras have been used in conjunction with schlieren imaging to visualize the shock propagation through the polymers with different pressure loads to determine the Hugoniot states [7, 8]. The shock velocity was extracted from high-speed images and particle velocity was calculated based on measured input pressure and experimentally measured shock velocity [7, 8]. Calculating particle velocity using pressure and shock velocity limit the particle velocity to a single velocity measurement. Velocity interferometry techniques, however, allow for the particle velocity history of a surface to be measured as a function of time. Early velocity interferometry techniques include Velocity Interferometry System for Any Reflector (VISAR) [2] and the Fabry–Pérot interferometer [19]. The modern technique of Photonic Doppler Velocimetry (PDV) is widely used in the literature today [10, 20–22]. This technique is highly flexible allowing for accurate measurements of velocities ranging from 1 to 1000 m/s with temporal resolutions as low as nanoseconds.

Particle velocity history yields the shock pulse shape and duration which vary based on the shock wave source. Planar impact tests impart a one-dimensional (1D) square shock pulse with a duration proportional to the flyer plate thickness. Whereas the shock imparted by an explosive point source yields a spherical shock profile with an instantaneous jump and a subsequent exponential decay [22]. Shock pressure decay in detonator loaded PMMA has been measured at distances of 0–10 mm from an explosive source [22], which yielded an initial rapid decay in peak shock pressure within the first 2 mm of shock propagation, followed by a slower decay in the next 8 mm. The concept of this decay behavior was explored by Duvall [23], where the shock pressure

ultimately decays to an elastic wave at large distances from the source.

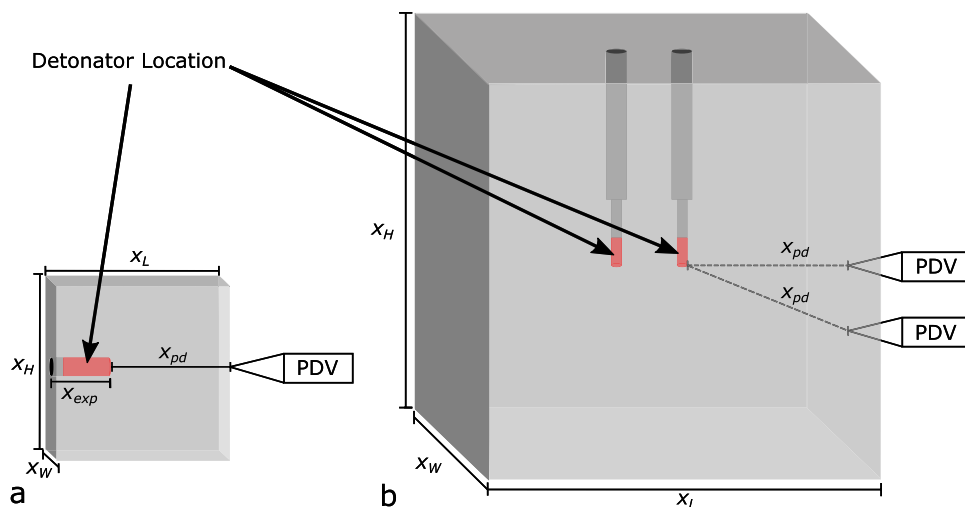
The present work examines explosively driven shock through PMMA to extend shock studies to spherical shock profiles. The shock response of detonator loaded PMMA was explored at distances greater than 10 mm from the explosive source to extend upon the previous research [22]. RP-80 EBW detonators were utilized here as the shock wave source because the size of the RP-80 allowed for the experimental scale of interest, they are highly repeatable, and to connect to the previous literature where they were also used [22]. To experimentally quantify the explosively driven shock state of PMMA at multiple locations from the explosive source high-speed schlieren imaging and PDV were implemented. PDV was used to measure the free surface velocity history and shock wave profile evolution at these varied distances. Free surface velocity is converted to particle velocity and correlated with the high-speed schlieren imaging data.

## Experimental Methods

PMMA configurations studied here are classified as near-field and far-field experiments based on the physical sample size and shock wave propagation distance. RP-80 electronic bridge-wire (EBW) detonators were used as the explosive source for all experiments. RP-80 EBW detonators are used here because of their high consistency of explosive material, explosive material press density, and their initiation. The EBW detonators contain 80 mg of pentaerythritol tetranitrate (PETN) as the initiating explosive and 123 mg of RDX (hexagen) as the output explosive yielding a total explosive mass of 203 mg, with a total energy output of about 1.14 kJ. The typical aluminum detonator cup was replaced here with Delrin for a better impedance match between the EBW detonator and the PMMA. The detonators were purchased from Teledyne Defense Electronics (part number 188-7072). The EBW detonator was detonated using an FS-17 fire-set.

Near-field (NF) tests implemented PMMA samples in which the height and width were the same for all tests. The height,  $x_H$ , was 76.2 mm and the width,  $x_W$ , was 25.4 mm as shown in Fig. 1a. Three nominal sample lengths were tested 48.7 mm, 73.6 mm, and 99.5 mm. A 25.4 mm deep hole,  $x_{exp}$ , was drilled in the sample for the detonator thus the PDV measurements were taken for nominal propagation distances ( $x_{pd}$ ) of 23.3 mm, 48.2 mm, and 74.1 mm from the explosive source. The hole for the explosive source was milled in one of the side faces, centered vertically. The RP-80 detonator was placed into the hole then a 5-min epoxy was placed on the back of the detonator to secure it in place. The sample width was less than the nominal propagation distances for 48.2 mm and 74.1 mm which potentially introduced free surface boundary interactions. For determination of free surface

**Fig. 1** Schematics of **a** near-field PMMA testing sample and **b** far-field PMMA testing sample



boundary effects, cubes of PMMA ( $x_L = x_H = x_W = 76.7$  mm) with the same hole assembly described above were also tested. The cube-like samples had a nominal propagation distance of 51.3 mm.

The far-field (FF) particle velocity experiments utilized a 305 mm  $\times$  305 mm  $\times$  305 mm PMMA cube (Fig. 1b). Two holes were drilled into the sample 29.2 mm off center with a distance between the holes of 58.4 mm. The hole depth for the epoxied explosive source was 165 mm. The far-field test contained two RP-80 EBW detonators, however, for the present research the shock from the explosive source closest to the PDV measurement in Fig. 1b was only of interest. The separation distance between the two explosive sources was large enough that the shock waves do not interact on the timescale of interest therefore, the results presented here were not impacted [24].

### PDV Measurement of Surface Motion

PDV is a light interferometry technique which is used to detect surface motion. The infrared light from the PDV system is reflected or scattered from a diffusely reflective moving surface causing the light to be Doppler-shifted. The reflective surface used here was retroreflective tape. The PDV arrangement was the heterodyne method described by Strand [25] meaning, the surface movement was observed as a beat frequency between the Doppler-shifted light and a reference laser of a different (heterodyne) frequency. The frequency difference between the working laser and the reference laser was set to 1 GHz.

The PDV measurements presented here were oriented normal to the surface being measured. For the near-field tests the measurement surface was the PMMA surface opposite the side where the detonator was loaded. The PDV probe was aligned with the center of the detonator face directed at the free surface as depicted in Fig. 2a. The far-field

measurements were recorded using a single PMMA sample with two PDV probes directed at the free surface. The first PDV probe was 165 mm from the top of the cube aligning the probe with the detonator. The second PDV probe was 50.8 mm below the first probe as shown in Fig. 1b. The first PDV probe was aligned such that the apparent velocity is parallel to the wave propagation direction thus no correction is required. The same is not true for the second PDV probe. The wave impacts the free surface at an angle of approximately  $22^\circ$  from horizontal. Geometric corrections were applied to account for the non-planar impact captured at the second location. Note that the geometric correction yields less than a 1% difference from the measured value to the corrected value for the impact at this  $22^\circ$  angle.

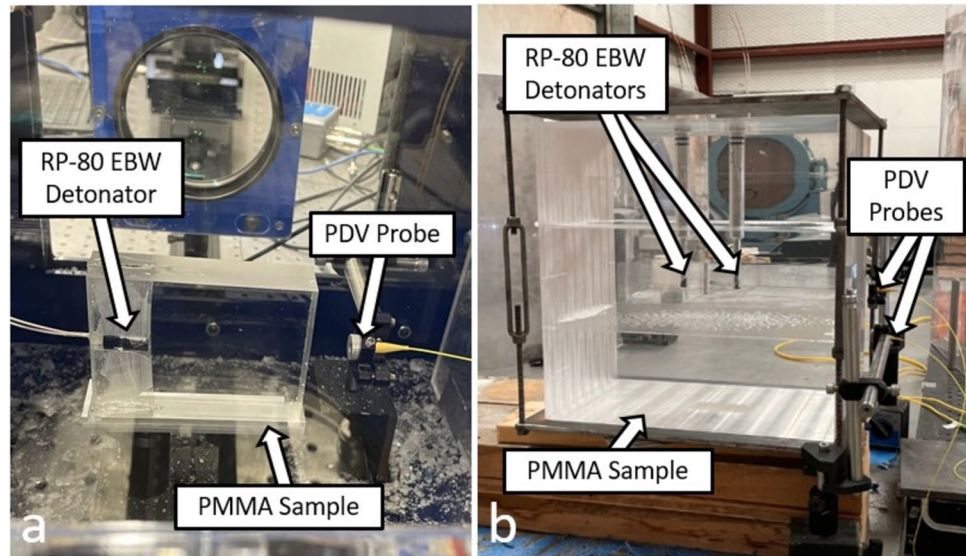
The PDV probes were purchased from OZ Optics and had a focal length of 20 mm. The focal length sets the distance from the free surface to the probe location. The heterodyne system was a Coherent Solutions LaserPXIe 1000 series connected to a DSA70804C oscilloscope sampling at a rate of 25 Gs/s for a duration of 180  $\mu$ s. The oscilloscope recorded the beat frequency and through post-processing was converted to particle velocity history.

PDV signals were post-processed using SIRHEN (Sandia InfraRed HETrodyne aNalysis) a data reduction software developed by Sandia National Laboratories [26]. The signal was processed for a duration of 100  $\mu$ s with 1000 data points producing free surface velocity output every 0.1  $\mu$ s. Surface velocity,  $u_{fs}$ , was converted to particle velocity,  $u_p$ , in the shock wave using  $u_p = \frac{u_{fs}}{2}$ .

### High-Speed Refractive Imaging

High-speed schlieren and shadowgraph imaging [16] were implemented to visualize the shock wave propagation through the samples. Visualization of the wave propagation allowed for the shock location to be measured as a function

**Fig. 2** Image of PDV aligned with the PMMA sample for **a** near-field testing 76.2 mm from the explosive source and **b** far-field testing 123.2 mm and 133.3 mm from the source



of time, and ultimately the shock velocity as a function of location through the block. The imaging systems consisted of a light source, a collimating optic, a focusing optic, and a high-speed camera. The schlieren imaging system included a knife-edge cut-off at the focal point of the focusing optic prior to the camera. Omitting the knife-edge cut-off produces focused shadowgrams. The test section was the area between the collimating optic and the focusing optic (see Fig. 3) which was the location of the test samples. The test samples were arranged such that the direction of wave propagation was perpendicular to the optical axis. Due to the sample geometry, the near-field testing was imaged using a lens based schlieren imaging system with 700-mm-diameter,  $f/5$  lenses (Fig. 3a) whereas the far-field testing required a z-type shadowgraphy system (Fig. 3b) with 304.8-mm-diameter,  $f/6$  parabolic mirrors (Edmund optics part #32-276-533).

A Specialised Imaging SI-LUX spoiled coherence laser illumination system was used as the light source for both imaging systems. The laser had a wavelength of 640 nm and a bandpass filter of the same wavelength was placed in front of the camera. The bandpass filter allows for only the laser light to be imaged, reducing external illumination from the detonation. Minimization of pixel blur in the images was achieved by pulsing the laser at a 10 ns duration which was consistent for all tests. High-speed imaging was achieved with a Shimadzu HPV-X2 camera recording at a frame rate of 5 million frames per second (fps) and 1 Mfps for the near- and far-field testing, respectively. The near-field tests were contained in a “boom box” placed in the center of the test section between the schlieren lenses.

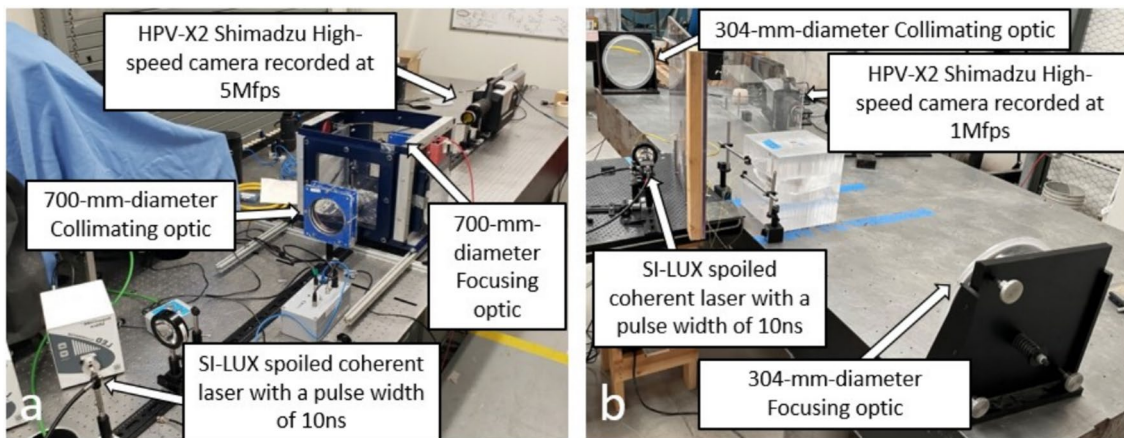


**Fig. 3** Images of the test set up for **a** the small-scale lens schlieren imaging and **b** the large-scale z-type schlieren imaging

## Experimental Results and Discussion

A series of tests were conducted for understanding the dynamic response of PMMA under explosive loading. The recorded free surface motion and high-speed schlieren/shadowgraph images allowed for the particle velocity and shock velocity to be experimentally determined.

### Free Surface Velocity Histories

The free surface movement is recorded through light interference, and the frequency information is converted to velocity using SIRHEN [26]. A representative power spectrum exported from the program is shown in Fig. 4a where the deviations from the baseline frequency indicate motion. The frequency with the peak intensity at each time was extracted representing the surface motion, which is shown in Fig. 4b. The heterodyne offset was removed and frequency was converted to velocity using the relation  $1000 \text{ m/s} = 1.29 \text{ GHz}$  yielding free surface velocity history. The initial jump in surface velocity indicates the shock arrival time,  $t_s$ . The absolute time was corrected,  $t_{ac}$ , such that  $t = 0$  was based on the detonator function time visualized in the schlieren images.

The free surface velocity histories experimentally measured for the NF and FF tests are shown in Fig. 5a. As expected, an increase in propagation distance corresponded

to a reduction in maximum surface velocity. The measured shock velocities indicate that the material response is likely elastic at the nominal propagation distances studied. Linear elastic waves will decay self similarly, therefore the PDV traces were aligned such that time zero was when the shock reached the free surface,  $t_n$ , presented in Fig. 5b. The graph shows that along with the amplitude change, which is expected, the shock pulse duration also varies. The variation in pulse shape is a function of the detonator explosive loading and release process, as well as some potential contributions from other effects such as geometry and the viscoelastic/viscoplastic response of PMMA [2, 5]. The gradual rounding up to the peak particle velocity has been attributed to the viscoelastic response of PMMA [2] which becomes more prevalent in the PDV traces as the propagation distance increases. There is a similar pulse shape between the 48.2 mm and 74.1 mm samples where the surface velocity reaches a maximum, begins to gradually decay, then experiences a rapid decay. The 23.2 mm, 123.2 mm, and 133.3 mm samples exhibit a more consistent decay implying that the rapid decay in the other two cases was due to sample geometry. The 48.2 mm and 74.1 mm samples have a sample width which is shorter than the propagation distance introducing boundary interactions.

To better understand the potential boundary effects caused by sample width being shorter than the propagation distance, cubic samples having a width longer than

**Fig. 4** Representative graphs of **a** spectrum created using SIRHEN and **b** The peak intensity information as a function of time from the power spectrum of **a**. This data is from a test at the 48.0 mm propagation distance

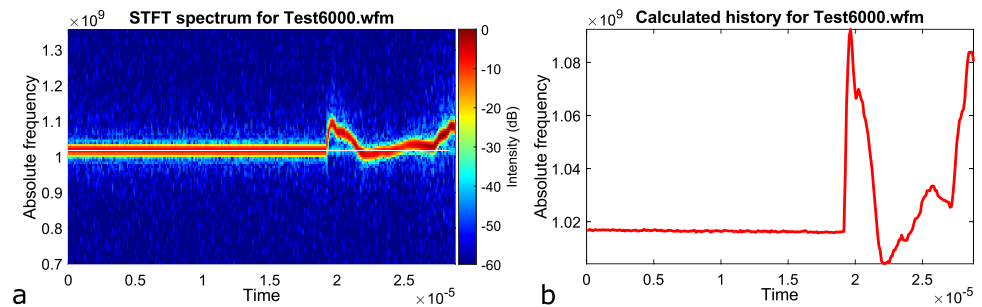
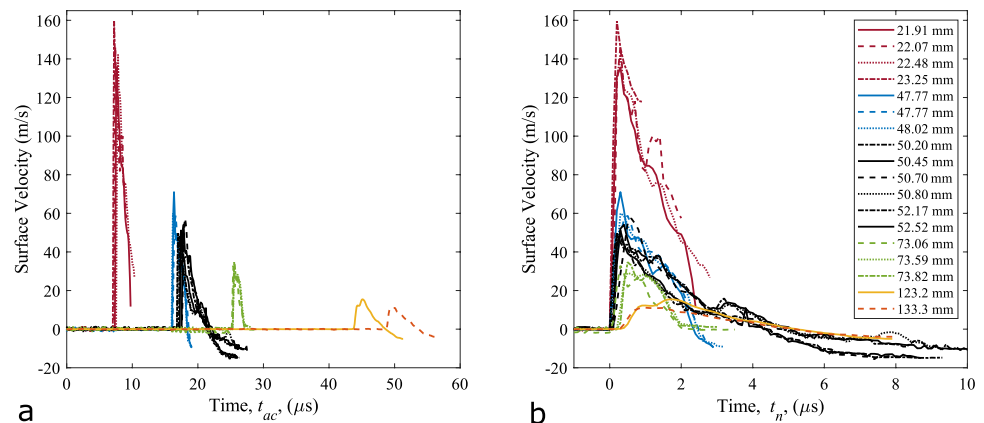


**Fig. 5** Free surface velocity history for the propagation distances studied where **a** has been corrected for detonator function time and **b** aligns the PDV trace based on the time the shock arrives at the free surface

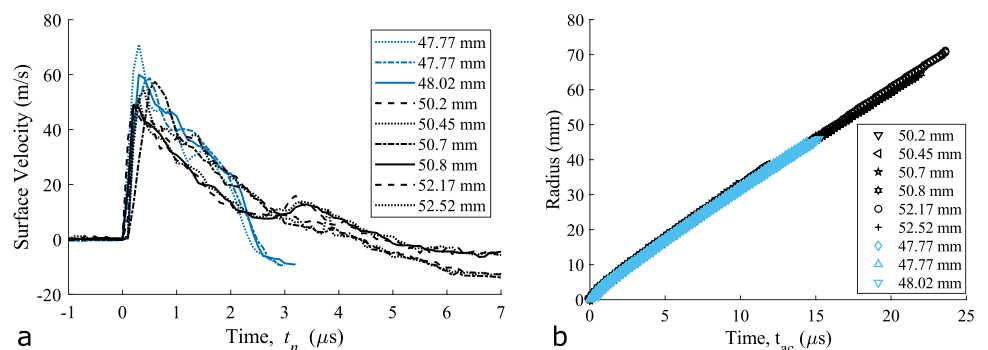


the propagation distance were tested and compared to the NF PDV traces. Figure 6a shows a comparison between the velocity history for the cubic samples (black lines) and the NF samples (blue lines). Since the propagation distance was slightly longer for the PMMA cubes the time was corrected by shifting the data to have a consistent shock arrival time at the free surface,  $t_n$ . The maximum surface velocities for the NF tests are slightly higher than the cubic tests, with the maximum recorded velocity being approximately 71.00 m/s and the lowest recorded velocity being 58.80 m/s. The cube tests had maximum and minimum recorded velocities of 57.72 m/s and 48.48 m/s, respectively. The variation in the recorded peak surface velocities was due to the cubic samples having a slightly longer propagation distance. The larger propagation from the spherical source allowed for the shock to decay to a lower velocity. The shock radius as a function of time extracted from the schlieren images for the cube samples (black points) and NF samples (blue points) shown in Fig. 6b were also compared. There is no observed difference in the shock radius as a function of time between the two geometries.

The maximum surface velocity recorded in the experiments were not impacted by boundary interactions, however, the two sample geometries show a difference in the decay after the shock impacts the free surface. Initially, all tests follow the same trend, but at about  $1 \mu\text{s}$  the NF trace begins to decay more rapidly and goes negative approximately  $2 \mu\text{s}$  prior to the cube samples going negative. The cube sample decay behavior is smoother than the decay behavior captured in the NF samples. The difference in decay behind the shock pulse is likely a result of wave reflections and release waves from side wall boundaries arriving at the measurement location.

Through comparison of the cubic samples and the NF samples it was determined that the peak surface velocities presented in Fig. 5 are accurate measurements. The experimental peak surface velocities were used to calculate the explosively driven particle velocities. The corresponding shock velocities were experimentally measured using the high-speed images.

**Fig. 6** Comparison of **a** free surface velocity histories and **b** shock radius as a function of time for the cubic PMMA samples and the NF samples. The data presented in black indicate the cube samples and the data presented in blue indicate the NF samples



## Shock Position Versus Time

A representative set of schlieren images showing the explosively driven shock propagation through the PMMA sample is presented in Fig. 7. Digital streak images were created to

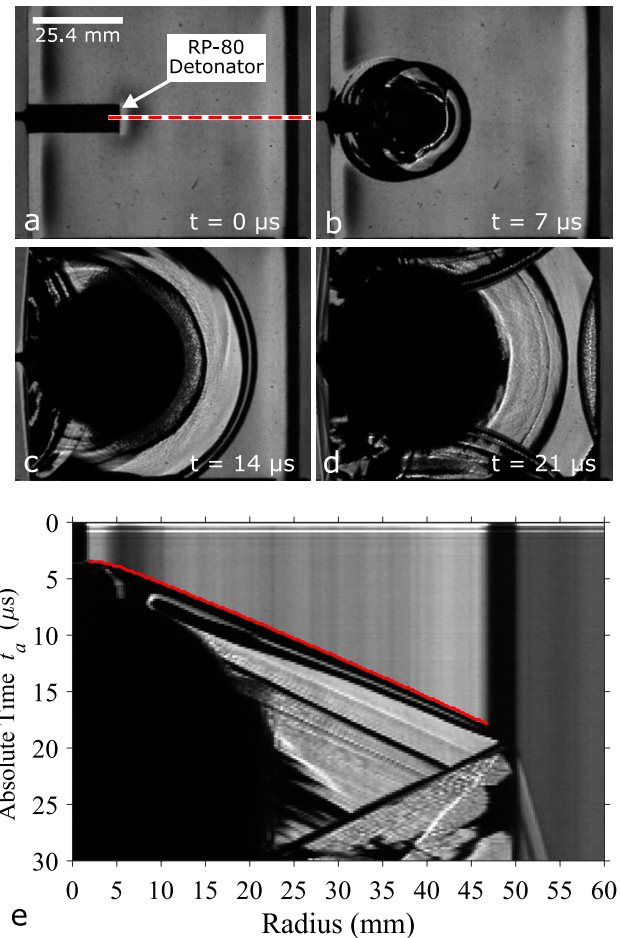


**Fig. 7** **a–d** Schlieren images of the shock wave imparted into a NF PMMA sample with a 48.02 mm propagation distance. The red dashed line in **a** represents the centerline of the detonator. The time shown on each image was corrected based on the detonator function time. **e** Shows a digital streak image created using the schlieren images. The shock front is identified and highlighted by the red line

visualize the shock wave propagation as a function of time [27] for each image set. The red dashed line in Fig. 7a indicates the row of pixels extracted from each image in the data set. The extracted rows of pixels were stacked vertically to create the digital streak image (Fig. 7e) such that time is on the y-axis, and distance is on the x-axis. The location of the shock front versus time, red line in Fig. 7e, was extracted and used to determine the shock velocity. For this analysis, the row of pixels used to create the streak images were selected based on the location of the PDV measurements. Note that optical distortions near the edge of the PMMA samples, likely due to residual stresses, cause the edge of the sample to not be optically transparent. This limits the optical measurement of the shock velocity measurement inside the sample.

Further analysis of the NF sample where the width was shorter than the propagation distance was preformed through comparison of the surface velocity history recorded using PDV to the digital streak image shown in Fig. 8. Four points, A–D, were selected to compare the surface velocity decay to the shock propagation visualized in the digital streak images. Points (B) ( $t = 1 \mu\text{s}$ ) through (D) ( $t = 3 \mu\text{s}$ ) were selected to compare the decay recorded in the PDV trace to the schlieren results. Point (C) corresponds to the approximate time that the NF sample and cube sample decay behavior deviates. Through comparison, the schlieren results show that at (B) a wave front from the free surface is visualized on the boundary indicating that the wave began to transmit into

free air. At time (C) there was no secondary wave visualized in the digital streak image indicating a change in decay behavior. This was expected as the schlieren imaging results were restricted to a two dimensional imaging plane and the decay behavior is a three dimensional effect. At point (D) the particle velocity history decay reaches a minimum corresponding to a change in the PMMA boundary visualized in the digital streak image which could be due to the stress state of the material changing with the increase in velocity shown subsequently after D in the PDV trace.

The maximum surface velocity, point (A) ( $t = 0 \mu\text{s}$ ) in Fig. 8, aligned with the time the shock impacts the free surface recorded in the high-speed image. The agreement between the PDV results and the schlieren imaging results, shown in Fig. 8, was further validation that it was appropriate to use the PDV results to determine the particle velocity corresponding to the shock wave velocity from the digital streak images.

The shock velocity corresponding to the PDV measurements were determined by extracting the shock radius as a function of time from the digital streak images using MATLAB. The extracted shock radius as a function of time for all test series are shown in Fig. 9a. A linear least-squares regression was used to determine the shock velocity corresponding to the propagation distances studied.

The shock velocity was determined by fitting a linear least squares regression to the data at the desired propagation distance. The linear fit was applied to each individual test, where the slope of the fits were averaged yielding the average shock velocity corresponding to the PDV data at the measured propagation distance. There was a slight non-linear behavior captured in the shock radius data, thus, the least-squares regression was applied to time windows of  $2 \mu\text{s}$  for propagation distances below 70 mm and  $4 \mu\text{s}$  for propagation distances above 70 mm. The window size for the fit was different above and below 70 mm due to limited shock radius data above 70 mm. Representative graphs showing the raw data and linear fit for propagation distances below and above 70 mm are presented in Fig. 9b, c respectively. The time was shifted such that  $t = 0$  was when the shock reached the propagation distance of interest. While the time shift was not strictly necessary, and had no impact on the slope, it allowed for a more direct visual comparison on the fitted data shown in Fig. 9b, c. Depending on the window size the shock radius data 1 or  $2 \mu\text{s}$  before and after the shock impacted the free surface was selected for the least-squares regression. Propagation distances below 70 mm utilized the data from the NF and cube tests for determination of the shock velocity whereas propagation distances above 70 mm utilized the data from the NF, cube, and FF tests. The FF tests were excluded from propagation distances below 70 mm because there was a larger uncertainty associated with the FF tests. The reason for utilizing all shock

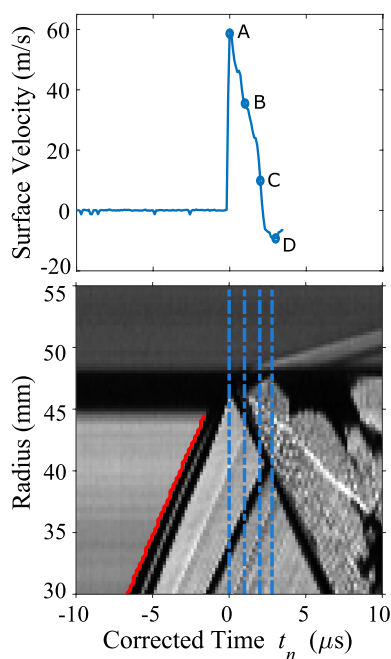
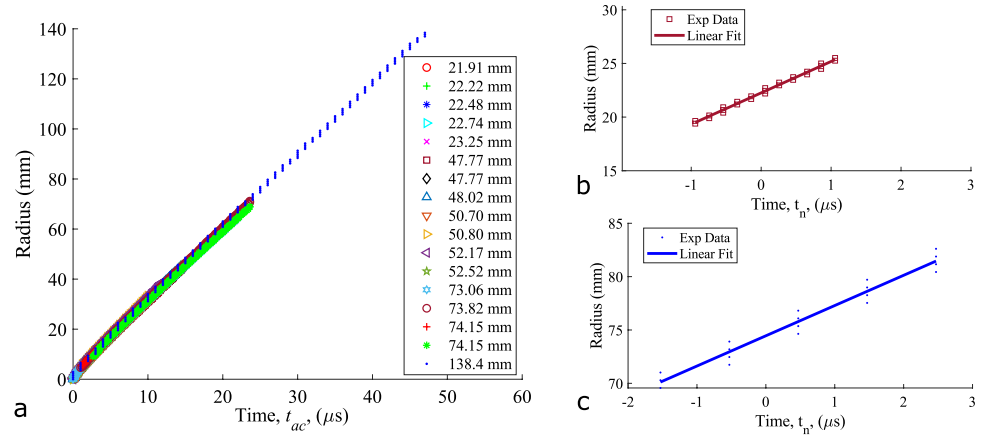


**Fig. 8** A digital streak image and the corresponding PDV trace for the NF PMMA sample having a propagation distance of 48.02 mm. Points A–D correspond to **A**  $0 \mu\text{s}$ , **B**  $1 \mu\text{s}$ , **C**  $2 \mu\text{s}$ , and **D**  $3 \mu\text{s}$

**Fig. 9** **a** Shock radius as a function of time extracted from the schlieren images and least squares linear fit for **b** a propagation distance of 22.48 mm over a 2  $\mu$ s window and **c** a propagation distance of 74.15 mm over a 4  $\mu$ s window



radius data that corresponds to the propagation distance was due to the sample boundary not being optically transparent thus shock radius data was not gathered near the sample boundary. Furthermore, the extent of the residual stresses distorting the sample boundary varied from test to test yielding an inconsistency when utilizing a single test for shock velocity determination. A summary of the time of arrival, particle velocity ( $u_p$ ), and shock velocity ( $U_s$ ) are presented in Table 1.

The least-squares fit uncertainty was calculated as outlined in [28]. Shock velocity values below a propagation distance of 70 mm were calculated using multiple data sets, thus, the uncertainty was based on the uncertainty of the average least-squares slope fits. The reported shock velocities above a propagation distance of 70 mm were from a single data set, thus, the reported uncertainty was based on the least-squares slope fit uncertainty. The uncertainty in the data for propagation distance of 70 mm was significantly larger than values below

**Table 1** Summary of explosively loaded PMMA shock parameters for propagation distances of 22.4–133.3 mm

Sample geometry	Propagation distance, $x_{pd}$ , (mm)	Time of arrival, $t_{ac}$ , ( $\mu$ s) <sup>1</sup>	Particle velocity, $u_p$ , (m/s)	Shock velocity, $U_s$ , (mm/ $\mu$ s)	Stress, $\sigma$ , (MPa)
NF	21.91 $\pm$ 0.13	7.34 $\pm$ 0.22	67.80 $\pm$ 0.14	2.96 $\pm$ 0.02	234 $\pm$ 16
NF	22.07 $\pm$ 0.13	7.09 $\pm$ 0.22	73.33 $\pm$ 0.15	2.96 $\pm$ 0.02	253 $\pm$ 19
NF	22.22 $\pm$ 0.13	–	–	2.96 $\pm$ 0.02	–
NF	22.48 $\pm$ 0.13	7.53 $\pm$ 0.22	71.10 $\pm$ 0.14	2.96 $\pm$ 0.02	245 $\pm$ 17
NF	22.74 $\pm$ 0.13	–	–	2.96 $\pm$ 0.02	–
NF	23.25 $\pm$ 0.13	7.03 $\pm$ 0.22	79.77 $\pm$ 0.16	2.95 $\pm$ 0.02	275 $\pm$ 20
NF	47.77 $\pm$ 0.13	15.96 $\pm$ 0.22	35.50 $\pm$ 0.07	2.78 $\pm$ 0.06	116 $\pm$ 13
NF	47.77 $\pm$ 0.13	16.12 $\pm$ 0.22	29.40 $\pm$ 0.06	2.78 $\pm$ 0.06	96 $\pm$ 11
NF	48.02 $\pm$ 0.13	15.99 $\pm$ 0.22	29.98 $\pm$ 0.06	2.78 $\pm$ 0.06	97 $\pm$ 13
Cube	50.20 $\pm$ 0.12	16.92 $\pm$ 0.22	24.24 $\pm$ 0.05	2.79 $\pm$ 0.06	79 $\pm$ 10
Cube	50.45 $\pm$ 0.12	–	27.08 $\pm$ 0.05	2.80 $\pm$ 0.06	89 $\pm$ 10
Cube	50.70 $\pm$ 0.12	17.45 $\pm$ 0.22	28.71 $\pm$ 0.06	2.80 $\pm$ 0.06	94 $\pm$ 11
Cube	50.80 $\pm$ 0.17	16.80 $\pm$ 0.22	24.47 $\pm$ 0.05	2.79 $\pm$ 0.06	80 $\pm$ 10
Cube	52.17 $\pm$ 0.17	16.70 $\pm$ 0.22	24.83 $\pm$ 0.05	2.82 $\pm$ 0.06	82 $\pm$ 9
Cube	52.52 $\pm$ 0.17	17.14 $\pm$ 0.22	25.58 $\pm$ 0.05	2.82 $\pm$ 0.06	84 $\pm$ 11
F/FF	73.06 $\pm$ 0.13	24.91 $\pm$ 0.22	16.44 $\pm$ 0.03	2.72 $\pm$ 0.46	52 $\pm$ 9
NF/FF	73.59 $\pm$ 0.13	25.09 $\pm$ 0.22	14.52 $\pm$ 0.03	2.72 $\pm$ 0.52	46 $\pm$ 9
NF/FF	73.82 $\pm$ 0.13	25.04 $\pm$ 0.22	17.35 $\pm$ 0.03	2.72 $\pm$ 0.54	55 $\pm$ 11
NF/FF	74.15 $\pm$ 0.13	–	–	2.84 $\pm$ 0.35	–
FF	123.2 $\pm$ 1.6	43.70 $\pm$ 1.00	7.73 $\pm$ 0.02	2.90 $\pm$ 0.36	26 $\pm$ 3
FF	133.3 $\pm$ 1.6	48.70 $\pm$ 1.00	5.15 <sup>2</sup> $\pm$ 0.01	2.66 $\pm$ 0.46	16 $\pm$ 3

<sup>1</sup> Corrected for detonation time based on schlieren images

<sup>2</sup> Geometric correction applied



70 mm because there were less tests replicated and the uncertainty associated with the FF tests was larger than the NF tests due to the scale relative to the camera resolution. Due to these differences, as the propagation distance increases so does the uncertainty. The uncertainty in the particle velocity was based on that explored by [20] in conjunction with an uncertainty analysis based on the shock angle impacting the free surface when the PDV probe was  $\pm 1.8$  mm off center line.

Table 1 also includes propagation distances, arrival time, and stress with their associated uncertainty. The propagation distance uncertainty was based on the sample length and hole depth. The uncertainty in arrival time was based on the detonator function time visualized in the high-speed images, where the exposure is 200 ns, and the PDV uncertainty. The stress uncertainty was a function of the uncertainty associated with the shock velocity, particle velocity, and PMMA density. Relative to the repeatability of the experiments, the RP-80 EBW detonators are highly repeatable however it is suspected that the placement of the detonators epoxied into the PMMA samples was the most significant source of variability. Figures 5 and 6 show that the surface velocity histories are similar for sample geometries and propagation distances that are nominally the same. The standard deviation for the particle velocities presented in Table 1 for the nominal propagation distances of 23.2 mm, 48.2 mm, 51.3 mm and 74.1 mm were 4.3 m/s, 2.7 m/s, 1.6 m/s, and 1.2 m/s respectively. The particle velocity standard deviation decreases with increased propagation distance. The variability in the particle velocities is attributed to the variability in epoxying the detonator into the PMMA samples. The shock velocities in Table 1 are not impacted by the epoxy induced variations the same as the particle velocities since the shock velocity values are averaged from all of the data collected. Furthermore, the shock radii presented in Fig. 9 are in good agreement across all experiments.

The attenuation behavior of a material is dependent on the stress state of the material. Here three classifications of the material response are considered, plastic, elastic, and elastic–plastic [29]. Plastic response of a material occurs at high pressures where the elastic portion of the response can be neglected, below that regime there is the elastic–plastic behavior where a material will behave both plastically and elastically. There is a maximum amount of stress which a material will behave purely elastic which is the Hugoniot Elastic Limit (HEL) of the material. In solids, the amplitude of spherical elastic waves decay with a  $r^{-1}$  behavior [30]. The shock parameters in Table 1 and the measured density ( $\rho_0$ ) of the PMMA were used to calculate stress ( $\sigma$ ) using conservation of momentum [29].

$$\sigma = \rho_0 u_p U_s \quad (1)$$

The maximum pressure in all tests presented here was less than the elastic limit of PMMA, where the HEL of PMMA

is in the range of 0.7–0.8 GPa [5], indicating the material response was elastic. To better understand the material behavior a trend line was fit to the particle velocity versus distance data and compared to the explosively loaded material response reported by Murphy et al. [22] in Fig. 10. The trend line fit to the data was  $u_p = 3.32r^{-1.23}$ . This has an exponent that is slightly more negative than expected for an elastic wave ( $r^{-1}$ ). This deviation from the elastic wave propagation is hypothesized to be caused by the viscoelastic behavior of PMMA. The particle velocity histories measured here were observed to have a more gradual particle velocity increase after the shock, rather than the immediate jump increase, which has been identified as a characteristic of a viscoelastic material response [2]. The explosively driven spherical shock waves cause the particle velocity decay behind the shock, which further causes the expected elastic peak particle velocity to not be achieved. These combined effects result in the slope of the fit equation being more negative. PMMA has been observed to act viscoelastically in nonlinear regions of the shock Hugoniot [2, 5], which is the area where these experiments are performed. There was a divergence between the trend line fit and the data collected by Murphy et al. [22] as the distance from the explosive source was reduced below about 2 mm, which aligns with the change in the shock behavior noted by Murphy et al. [22]. Murphy et al. also reported a jump velocity and a maximum velocity which is not discussed here, furthermore, in the present comparison only the maximum velocity was reported [22].

In Fig. 11 the explosive response of PMMA measured here, and explored by Murphy et al. [22] were compared to the classical experiments of Barker and Hollenbach [2] and Jordan et al. [10] for PMMA under planar impact

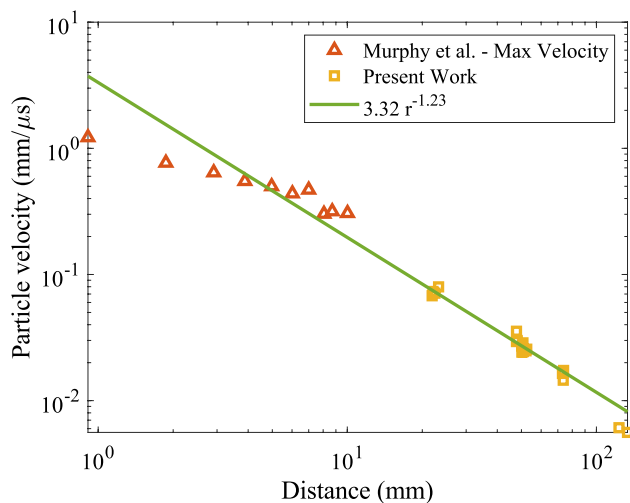
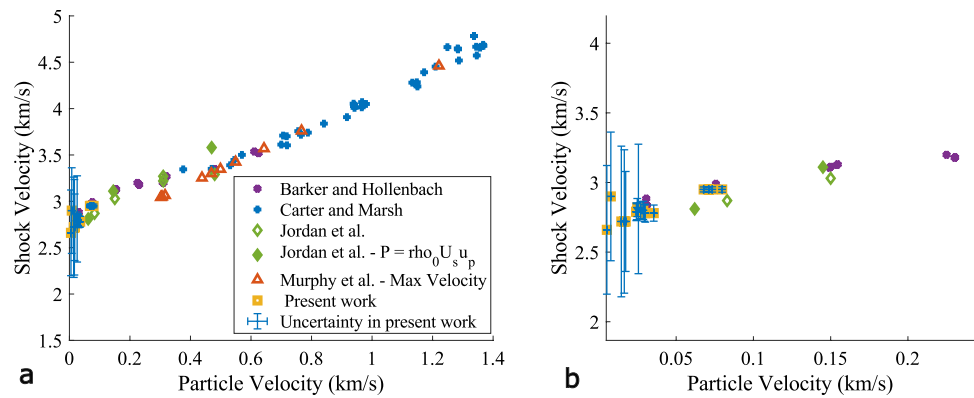


Fig. 10 Logarithmic plot of particle velocity vs radius for explosively loaded PMMA

**Fig. 11** Shock Hugoniot for PMMA from explosively loaded materials and impact experiments conducted by Barker and Hollenbach [2], Carter and Marsh [8], Jordan et al. [10], and Murphy et al. [22] where **b** is a zoomed in section of **a**



loading. The shock velocity corresponding to the particle velocity measurements made by [22] are calculated using  $U_s = 2.577 + 1.543u_p$  (for  $u_p < 2.415 \text{ mm}/\mu\text{s}$ ) as determined by [22]. Shock and particle velocities reported by [2] and [10] were experimentally measured. In some cases Jordan et al. [10] measured only the particle velocity and used Eq. 1 to determine shock velocity indicated as the solid points in Fig. 11.

Barker and Hollenbach implemented a Michelson interferometer technique and velocity interferometer for the determination of particle velocity. Shock velocity was measured using light beams to determine the time of target impact and the time at which the shock impacts the sample free surface, further details are found in [2]. Jordan et al. recorded shock velocity by the implementation of manganin gauges in the sample and particle velocity was determined using PDV.

The present work explored spherical shock wave behavior where experimental shock velocities and particle velocities were measured. There were relatively larger uncertainties in the shock velocities for the lower particle velocities since they correspond to a propagation distance above 70 mm. Note that the error bars for the shock velocities from the NF tests are significantly smaller, due to a reduced uncertainty, which are on the order of the symbol size. The measured values of shock and particle velocities agree with the values reported by [2] and [10] which are planar one dimensional shock results. The explosively-driven shock wave and impact-induced shock wave thus propagate in a similar manner through the PMMA. The present work extends the region in which explosively-driven shock waves in PMMA have been explored.

## Conclusions

The explosively driven shock response of PMMA at varied distances from an explosive source was experimentally characterized using high-speed schlieren imaging and PDV. High-speed imaging was implemented to visualize

the shock response of the material, where shock velocity was extracted. Agreement between velocities determined using PDV and the high-speed images were presented. The shock velocities corresponding to the measured free surface velocities were determined from the schlieren images. The free surface velocity histories revealed geometric effects in the sample with nominal propagation distances of 48.2 mm and 74.1 mm likely due to effects of lateral free surface internal shock reflections which will be investigated in the future. The PMMA response was fit to a decay equation having a slightly more negative exponent compared to an elastic decay response at the studied distances. The wave loses the majority of its strength within the first 16  $\mu\text{s}$ , approximately 48 mm, of propagation.

The present work was compared to previously published data, extending the space where explosively-driven shock wave propagation in PMMA was experimentally measured. The explosively driven spherical shock waves in PMMA result in a material response that is consistent with the response measured in planar impact induced shock experiments at low particle velocities. This is despite significant differences in the mechanics of wave propagation i.e. the attenuation in the explosively driven spherical shock waves. This is likely because the amplitude of the waves presented in this manuscript all fall in the elastic regime, where the attenuation in the spherical wave case does not cause a transition from the strong shock regime to the elastic regime.

**Acknowledgements** Portions of this work were supported by Sandia National Laboratories PO 2179527, DOE-NNSA MSIPP award DE-NA0003988, and AFOSR Grant FA9550-19-1-0379. Sandia National Laboratories is a multimission laboratory managed and operated by National Technology and Engineering Solutions of Sandia, LLC., a wholly owned subsidiary of Honeywell International, Inc., for the U.S. Department of Energy's National Nuclear Security Administration under contract DE-NA-0003525.

**Funding** Open access funding provided by SCELCC, Statewide California Electronic Library Consortium.

## Declarations

**Conflict of interest** The authors have no conflicts to declare.

**Open Access** This article is licensed under a Creative Commons Attribution 4.0 International License, which permits use, sharing, adaptation, distribution and reproduction in any medium or format, as long as you give appropriate credit to the original author(s) and the source, provide a link to the Creative Commons licence, and indicate if changes were made. The images or other third party material in this article are included in the article's Creative Commons licence, unless indicated otherwise in a credit line to the material. If material is not included in the article's Creative Commons licence and your intended use is not permitted by statutory regulation or exceeds the permitted use, you will need to obtain permission directly from the copyright holder. To view a copy of this licence, visit <http://creativecommons.org/licenses/by/4.0/>.

## References

- Barker LM, Hollenbach RE (1965) Interferometer technique for measuring the dynamic mechanical properties of materials. *Rev Sci Instrum* 36(11):1617–1620. <https://doi.org/10.1063/1.1719405>
- Barker LM, Hollenbach RE (1970) Shock-wave studies of PMMA, fused silica, and sapphire. *J Appl Phys* 41(10):4208–4226. <https://doi.org/10.1063/1.1658439>
- Schuler KW (1970) Propagation of steady shock waves in polymethyl methacrylate. *J Mech Phys Solids* 18(4):277–293. [https://doi.org/10.1016/0022-5096\(70\)90008-6](https://doi.org/10.1016/0022-5096(70)90008-6)
- Asay JR, Barker LM (1974) Interferometric measurement of shock-induced internal particle velocity and spatial variations of particle velocity. *J Appl Phys* 45(6):2540–2546. <https://doi.org/10.1063/1.1663627>
- Millett JCF, Bourne NK (2000) The deviatoric response of polymethylmethacrylate to one-dimensional shock loading. *J Appl Phys* 88(12):7037–7040. <https://doi.org/10.1063/1.1324699>
- Lacina D, Neel C, Dattelbaum D (2018) Shock response of poly[methyl methacrylate] (PMMA) measured with embedded electromagnetic gauges. *J Appl Phys* 123(18):185901. <https://doi.org/10.1063/1.5023230>
- Marsh SP, Laboratory LAS.: LASL shock Hugoniot data. University of California Press, Berkeley. Stanley P. Marsh, editor
- Carter WJ, Marsh SP (1995) Hugoniot equation of state of polymers. Los Alamos National Lab. (LANL). LA-13006-MS
- Svingala FR, Hargather MJ, Settles GS (2012) Optical techniques for measuring the shock Hugoniot using ballistic projectile and high-explosive shock initiation. *Int J Impact Eng* 50:76–82. <https://doi.org/10.1016/j.ijimpeng.2012.08.006>
- Jordan JL, Casem D, Zellner M (2016) Shock response of polymethylmethacrylate. *J Dyn Behav Mater* 2(3):372–378. <https://doi.org/10.1007/s40870-016-0071-5>
- Chapman DJ, Eakins DE, Williamson DM, Proud W (2012) Index of refraction measurements and window corrections for PMMA under shock compression. In: AIP conference proceedings. vol 1426. AIP, pp 442–445
- Bhowmick M, Basset WP, Matveev S, Salvati L, Dlott DD (2018) Optical windows as materials for high-speed shock wave detectors. *AIP Adv* 8:12. <https://doi.org/10.1063/1.5055676>
- Kister G, Wood DC, Appleby-Thomas GJ, Leighs JA, Goff M, Barnes NR et al (2014) An overview on the effect of manufacturing on the shock response of polymers. *J Phys Conf Ser* 500(19):192022. <https://doi.org/10.1088/1742-6596/500/19/192022>
- Siviour CR, Jordan JL (2016) High strain rate mechanics of polymers: a review. *J. Dyn Behav Mater* 2(1):15–32. <https://doi.org/10.1007/s40870-016-0052-8>
- Field JE, Walley SM, Proud WG, Goldrein HT, Siviour CR (2004) Review of experimental techniques for high rate deformation and shock studies. *Int J Impact Eng* 30(7):725–775. <https://doi.org/10.1016/j.ijimpeng.2004.03.005>
- Settles GS., Gary S (2001) Schlieren and shadowgraph techniques: visualizing phenomena in transparent media. Springer, Berlin
- Tobin JD, Hargather MJ (2016) Quantitative schlieren measurement of explosively-driven shock wave density, temperature, and pressure profiles. *Propellants Explos Pyrotech* 41(6):1050–1059. <https://doi.org/10.1002/prop.201600097>
- Hargather MJ, Settles GS (2012) A comparison of three quantitative schlieren techniques. *Opt Lasers Eng* 50(1):8–17. <https://doi.org/10.1016/j.optlaseng.2011.05.012>
- McMillan CF, Goosman DR, Parker NL, Steinmetz LL, Chau HH, Huen T et al (1988) Velocimetry of fast surfaces using Fabry–Perot interferometry. *Rev Sci Instrum* 59(1):1–21. <https://doi.org/10.1063/1.1140014>
- Jensen BJ, Holtkamp DB, Rigg PA, Dolan DH (2007) Accuracy limits and window corrections for photon Doppler velocimetry. *J Appl Phys* 101(1):013523. <https://doi.org/10.1063/1.2407290>
- Dolan DH (2020) Extreme measurements with photonic Doppler velocimetry (PDV). *Rev Sci Instrum* 91(5):051501. <https://doi.org/10.1063/5.0004363>
- Murphy MJ, Lieber MA, Biss MM (2018) Novel measurements of shock pressure decay in PMMA using detonator loading. In: AIP conference proceedings. vol. 1979, p 160020
- Duval GE (1962) Concepts of shock wave propagation. *Bull Seismol Soc Am* 52(4):869–893
- Torres SM, Vorobiev OY, Robey RE, Hargather MJ (2023) A study of explosive-induced fracture in polymethyl methacrylate (PMMA). *J Appl Phys*. <https://doi.org/10.1063/5.0160147>
- Strand OT, Goosman DR, Martinez C, Whitworth TL, Kuhlrow WW (2006) Compact system for high-speed velocimetry using heterodyne techniques. *Rev Sci Instrum* 77(8):083108. <https://doi.org/10.1063/1.2336749>
- Daniel Dolan I, Ao T (2010) SIRHEN: a data reduction program for photonic Doppler velocimetry measurements. SAND2010-3628
- Settles GS, Hargather MJ (2017) A review of recent developments in schlieren and shadowgraph techniques. *Meas Sci Technol* 28(4):042001. <https://doi.org/10.1088/1361-6501/aa5748>
- Taylor JR (John Robert) (1997) An introduction to error analysis: the study of uncertainties in physical measurements. Second edition. ed. Sausalito. University Science Books, California
- Cooper P (2018) Explosives engineering. Wiley, Hoboken
- Meyers (1994) Dynamic behavior materials. Wiley, Hoboken

**Publisher's Note** Springer Nature remains neutral with regard to jurisdictional claims in published maps and institutional affiliations.